

Numerical study of a Taylor bubble rising in stagnant liquids

Chang-Wei Kang, Shaoping Quan,^{*} and Jing Lou

Institute of High Performance Computing, 1 Fusionopolis Way, 16-16 Connexis, Singapore 138632, Singapore

(Received 15 September 2009; revised manuscript received 16 April 2010; published 17 June 2010)

The dynamics of a Taylor bubble rising in stagnant liquids is numerically investigated using a front tracking coupled with finite difference method. Parametric studies on the dynamics of the rising Taylor bubble including the final shape, the Reynolds number (Re_T), the Weber number (We_T), the Froude number (Fr), the thin liquid film thickness (w/D), and the wake length (l_w/D) are carried out. The effects of density ratio (η), viscosity ratio (λ), Eötvös number (Eo), and Archimedes number (Ar) are examined. The simulations demonstrate that the density ratio and the viscosity ratio under consideration have minimal effect on the dynamics of the Taylor bubble. Eötvös number and Archimedes number influence the elongation of the tail and the wake structures, where higher Eo and Ar result in longer wake. To explain the sudden extension of the tail, a Weber number (We_T) based on local curvature and velocity is evaluated and a critical We_T is detected around unity. The onset of flow separation at the wake occurs in between $Ar=2 \times 10^3$ and $Ar=1 \times 10^4$, which corresponds to Re_T between 13.39 and 32.55. Archimedes number also drastically affects the final shape of Taylor bubble, the terminal velocity, the thickness of thin liquid film, as well as the wall shear stress. It is found that $w/D = 0.32 Ar^{-0.1}$.

DOI: [10.1103/PhysRevE.81.066308](https://doi.org/10.1103/PhysRevE.81.066308)

PACS number(s): 47.85.-g, 47.55.dd

I. INTRODUCTION

A Taylor bubble is a long bullet-shaped bubble which nearly occupies the entire cross section of a liquid-filled tube, leading to the formation of a thin liquid film between the wall and the bubble [1]. Taylor bubbles can also be characterized as having a rounded leading edge, a cylindrical body with a length of several times of the bubble diameter and a trailing edge. The shape of the trailing edge can be flat, rounded, indented, or jagged depending on the flow conditions, liquid properties, and size and orientation of the tube. The shape at the rear of a Taylor bubble subsequently determines the patterns of the recirculating liquid therein.

Taylor bubbles are noted to present in a myriad of gas-liquid two-phase systems and this type of flow is of fundamental importance to many industrial applications, including hydrocarbon production in oil wells and their transportation in pipelines [2], heat exchanger, air-lift reactor [3], buoyancy-driven fermenters, emergency cooling of nuclear reactors [4], and coating technology and polymer processing [5]. This is because the distribution of gas bubbles in the tube significantly affects the hydrodynamics, heat transfer, and mass transfer. In addition, Bellara *et al.* [6] showed that introducing gas bubbles into hollow fiber membrane modules was one of the cost-effective ways to reduce concentration polarization and thus promotes permeate flux. Taylor bubbles also occur in physiological systems. Red blood cells separated by blood plasma are easily deformable under stresses and behave like Taylor bubbles in smaller blood vessels [7]. Prothero and Burton [8] pointed out that strong circulation ahead of red blood cells was very effective for nutrient distribution. The presence of gas bubbles in human vascular structures which is also called gas embolism, such as nitrogen bubble formation in diver's blood, can cause serious

sickness, and these bubbles usually have a sausage shape, i.e., similar to Taylor bubbles [9,10]. Large gas bubbles also appear in drilling systems. Rader *et al.* [11] studied factors that affect the bubble-rise velocity of a gas kick in an annulus. In view of the wide spectrum of applications, a great amount of research has been devoted to the study of this two-phase flow phenomenon in order to obtain a reliable understanding of the hydrodynamics of a Taylor bubble at its different regions, i.e., nose, thin liquid film, and wake.

From the literature, it is noted that over the past decades, theoretical analyses [12,13] and experimental studies [14–17] have been conducted to understand the behavior of Taylor bubbles rising in gas-liquid systems. An equation relating the terminal velocity of the bubble (U_T) with the gravitational force (g) and the tube diameter (D) by a constant value C (proposed by Dumitrescu [18]) is expressed as

$$U_T = C(gD)^{1/2}. \quad (1)$$

Some other investigations using analytical and/or experimental approaches are tabulated in Table I wherein each proposed a slightly different value for C .

Aside from the prediction and measurement of the terminal velocity of the rising Taylor bubble, the shear stress in

TABLE I. A collection of constant C obtained from the literature.

C	Methodology	Reference
0.328	Analytical	Davies and Taylor [1]
0.351	Analytical	Dumitrescu [18]
0.303	Analytical	Brown [19]
0.350	Experimental	Campos and Guedes De Carvalho [14]
0.328	Experimental	Laird and Chisholm [20]
0.351	Experimental	Polonsky <i>et al.</i> [21]

^{*}Corresponding author; quansp@ihpc.a-star.edu.sg

the liquid film and the flow in the wake of Taylor bubbles are also of interest for engineers and scientists, because the shear stresses in the thin film are important for depolarization by slug flow in tubular separation membranes [22] and the vortices in the wake region can enhance the liquid mixing in devices such as air-lift reactors [14]. In the study of Nogueira *et al.* [15], the averaged velocity profiles in the thin liquid film were measured and from the velocity field, the shear stresses along the liquid film were determined. The study showed that decreasing liquid viscosities results in the reduction in the wall shear stress. Campos and Guedes De Carvalho [14] did a photographic study of the flow in the wake of an individual Taylor bubble rising in a stagnant liquid. They identified three different flow patterns in the wake, namely, laminar, transitional, and turbulent. They also reported that the type of the flow pattern in the wake depends only on the inverse viscosity number N_f ($N_f = \rho_l g^{1/2} D^{3/2} / \mu_l$, where ρ_l is the density of the surrounding fluid, g denotes the gravitational acceleration, D stands for the tube diameter, and μ_l is the viscosity of the surrounding fluid).

The experimental investigations and analytical analyses presented earlier have shed a light on the dynamics of a Taylor bubble rising in stagnant liquids. However, in order to visualize and characterize the flow field around and within Taylor bubble, numerical simulation would provide a better and cost-effective alternative. In addition, numerical approaches enable a systematic study that could isolate the importance of each governing parameter. Compared to the vast studies of Taylor bubbles by experimental and theoretical approaches, the numerical investigation is relatively limited. Kawaji *et al.* [23] employed a volume of fluid (VOF) method to simulate the hydrodynamics of a Taylor bubble rising through stagnant liquid in a vertical tube. Under the conditions simulated, the bubble of different lengths was found to have the same terminal speed. Bugg *et al.* [24] had demonstrated that by using VOF, it was possible to model several important features of steadily rising Taylor bubble. In the numerical study, the terminal speed of the bubble was well predicted. The film thickness and the average velocity in the film compared favorably with experimental data. Similar studies were also performed by Taha and Cui [4,7] and Ndinisa *et al.* [25]. The VOF method is robust and flexible but it is often excessively diffusive and the interface is smeared. Recently, Lu and Prosperetti [26] numerically studied Taylor bubble rising by neglecting the flow in the gas. In this paper, the front tracking method [27–29] is applied instead. In the front tracking method, the interface is tracked explicitly with the front velocity interpolated from the regular finite difference grid. The front tracking method deals with two-phase liquids and avoids the ambiguous gas-liquid interface reconstruction in VOF. The objective of this study is to investigate systematically the effects of the density ratio, the viscosity ratio, the Eötvös number, and the Archimedes number on the dynamics of the Taylor bubble, especially the terminal velocity, the wake length, and the wall shear stress.

II. PROBLEM DESCRIPTION AND SOLUTION STRATEGY

Figure 1 shows the computational domain used to investigate the behavior of a Taylor bubble rising. This problem is

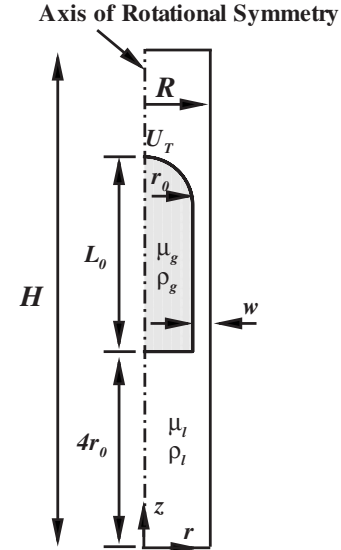


FIG. 1. Computational domain for simulating a Taylor bubble rising in stagnant liquids.

assumed to be of rotational symmetry (which others also refer to as three-dimensional axis symmetry), so a cylindrical coordinate (r, z) is employed for the simulations. The cylindrical tube of inner radius $R=0.016$ m and height $H=0.32$ m is closed on all sides. The Taylor bubble of radius r_0 is located at $4r_0$ from the bottom wall. The top wall is at a distance far away from the point of the release. This is to minimize the bottom and top wall effects on the rise of the Taylor bubble. In all the simulation cases, the radius of the Taylor bubble is fixed as $r_0=0.0135$ m and gravity is in the negative z direction.

A. Governing equations

In this numerical study, the fluids (both bubble and surrounding liquid) are assumed to be immiscible and incompressible. The incompressibility assumption implies that the mass conservation equation can be expressed as

$$\nabla \cdot \mathbf{u} = 0. \quad (2)$$

The Navier-Stokes equation governing the momentum conservation for each fluid phase can be written as

$$\rho \left(\frac{\partial \mathbf{u}}{\partial t} + \nabla \mathbf{u} \cdot \mathbf{u} \right) = -\nabla p + \nabla \cdot \mu (\nabla \mathbf{u} + \nabla^T \mathbf{u}) + \mathbf{F}_{st} + \rho \mathbf{g}, \quad (3)$$

where \mathbf{u} denotes the fluid velocity; p is the pressure; ρ and μ are the fluid density and viscosity, respectively; \mathbf{g} is the gravitational acceleration; and \mathbf{F}_{st} are surface tension forces distributed near the interface.

The numerical simulation is initialized with the following condition:

$$\mathbf{u}(r, z, t = 0) = 0. \quad (4)$$

The boundary conditions for all the sidewalls are

$$\mathbf{u}(r, 0, t) = \mathbf{0}, \quad 0 \leq r \leq R, \quad (5)$$

$$\mathbf{u}(r, H, t) = \mathbf{0}, \quad 0 \leq r \leq R, \quad (6)$$

$$\mathbf{u}(R, z, t) = \mathbf{0}, \quad 0 \leq z \leq H. \quad (7)$$

The condition at the axis of rotational symmetry is expressed as follows:

$$\frac{\partial \mathbf{u}}{\partial r}(0, z, t) = \mathbf{0}, \quad 0 \leq z \leq H. \quad (8)$$

For the simulations, a uniform background grid of 64×1280 is employed (64 in the r direction and 1280 in the z direction). In addition, a constant Courant-Friedrichs-Lewy number of 0.05 is used.

In this study, a group of dimensionless numbers is adopted to characterize the behavior of Taylor bubble rising. These nondimensional parameters are the Eötvös number (Eo), the Archimedes number (Ar), the Reynolds number (Re_T), the Weber number (We_T), the Froude number (Fr), the density ratio (η), and the viscosity ratio (λ). They are defined as

$$\begin{aligned} \text{Eo} &= \frac{(\rho_l - \rho_g)gD^2}{\sigma}, & \text{Ar} &= \frac{\rho_l(\rho_l - \rho_g)gD^3}{\mu_l^2}, & \text{Re}_T &= \frac{\rho_l U_T D}{\mu_l}, \\ \text{We}_T &= \frac{\rho_l U_T^2 D}{\sigma}, & \text{Fr} &= \frac{U_T}{(gD)^{1/2}}, & \eta &= \frac{\rho_l}{\rho_g}, & \lambda &= \frac{\mu_l}{\mu_g}. \end{aligned}$$

In these groups, ρ_l and ρ_g are the densities of liquid and gas, respectively; g is the acceleration due to gravity; D is the tube diameter; σ is the surface tension coefficient; μ_l and μ_g are the dynamic viscosities of liquid and gas, respectively; and U_T refers to the terminal velocity of a bubble. Other commonly used dimensionless parameters, such as the Morton number (Mo), the buoyancy Reynolds number (Re_B), and the inverse viscosity number (N_f), can be derived by manipulating and/or combining two or more of other nondimensional groups. For example, for Taylor bubble rising, $N_f = \text{Re}_B = \sqrt{\text{Ar}}$ and $\text{Mo} = \text{Eo}^3 / N_f^4$.

B. Numerical method

The Navier-Stokes equation is discretized on the staggered and structured grid using a finite-difference-based variable density projection method [30] and the time-stepping procedure is based on Crank-Nicholson method. In the projection method, an intermediate velocity \mathbf{u}^* is first obtained using a semi-implicit viscous procedure and solved by a multigrid method. The equation for calculating the intermediate velocity \mathbf{u}^* is given as follows:

$$\begin{aligned} \rho^{n+1/2} \left(\frac{\mathbf{u}^* - \mathbf{u}^n}{\Delta t} \right) &= - [(\mathbf{u} \cdot \nabla) \mathbf{u}]^{n+1/2} - Gp^{n-1/2} \\ &+ \left(\frac{D(\mathbf{u}^*) + D(\mathbf{u}^n)}{2} \right) + \mathbf{F}_{st}^{n+1/2} + \rho^{n+1/2} \mathbf{g}, \end{aligned} \quad (9)$$

where Gp represents the pressure gradient operator, $D(\mathbf{u}) = \nabla \cdot \mu(\nabla \mathbf{u} + \nabla^T \mathbf{u})$ represents the diffusion operator, and \mathbf{F}_{st}

represents the discretized surface tension forces. Subsequently, a projection method is invoked on the intermediate velocity \mathbf{u}^* to obtain \mathbf{u}^{n+1} . The projection step is given by the following equations:

$$\begin{aligned} \frac{\mathbf{u}^{n+1} - \mathbf{u}^n}{\Delta t} &= \mathcal{P} \left(\frac{\mathbf{u}^* - \mathbf{u}^n}{\Delta t} \right), \\ \frac{1}{\rho^{n+1/2}} Gp^{n+1/2} &= \frac{1}{\rho^{n+1/2}} Gp^{n-1/2} + (I - \mathcal{P}) \left(\frac{\mathbf{u}^* - \mathbf{u}^n}{\Delta t} \right), \end{aligned} \quad (10)$$

where \mathcal{P} represents the discretization of the projection operator. The details such as methods adopted to evaluate the advection and diffusion terms are given in [28] and steps involved in discretization of individual terms in Eqs. (9) and (10) for a rotational symmetric case and the corresponding time-step restrictions are presented in [31].

In Eq. (9), the material properties such as density and viscosity of the single continuum fluid are calculated using the following equations:

$$\rho(r, z, t) = \rho_l I(r, z, t) + \rho_g [1 - I(r, z, t)], \quad (11)$$

$$\frac{\rho}{\mu(r, z, t)} = \frac{\rho_l}{\mu_l} I(r, z, t) + \frac{\rho_g}{\mu_g} [1 - I(r, z, t)], \quad (12)$$

where $I(r, z, t)$ is the Heaviside function used to smooth out the fluid properties across a finite thickness of the interface region, and subscripts l and g represent liquid and gas phases, respectively. $I(r, z, t)$ varies smoothly from 1 in the surrounding phase to zero in the dispersed phase (bubble) across the interface and the value of $I=0.5$ denotes the interface. $I(r, z, t)$ is computed by solving a Poisson equation, as given in Eq. (13) [32],

$$\nabla \cdot \nabla I(r, z, t) = \nabla \cdot \int_{S(t)} \mathbf{n}_f \delta(\mathbf{x} - \mathbf{x}_f) ds. \quad (13)$$

Here, $S(t)$ denotes a time-dependent interface, \mathbf{n}_f represents the unit normal vector on the interface pointing into the bulk fluid, \mathbf{x}_f denotes the position vector on the interface, and $\delta(\mathbf{x} - \mathbf{x}_f)$ stands for the delta function that is nonzero only when $\mathbf{x} = \mathbf{x}_f$. The one-dimensional δ function [33] is given as follows:

$$\delta(d) = \begin{cases} \delta_1(d), & |d| \leq 1 \\ 1/2 - \delta_1(d), & 1 < |d| < 2 \\ 0, & |d| \geq 2, \end{cases} \quad (14)$$

where $\delta_1(d) = (3 - 2|d| + \sqrt{1 + 4|d| - 4d^2})/8$ and d denotes the distance from the interface.

In addition, the surface tension forces \mathbf{F}_{st} are calculated by

$$\mathbf{F}_{st} = \int_{S(t)} \sigma \kappa \mathbf{n}_f \delta(\mathbf{x} - \mathbf{x}_f) ds, \quad (15)$$

and distributed to the computational grid in a ‘‘density-weighted’’ manner (for more details, see [28]). Here, s and κ are the arc length and curvature of the interface, respectively,

TABLE II. Simulation conditions and results.

Case	η	λ	Eo	Ar	Re_T	We_T	Fr	w/D	l_w/D
1	25	100	196	4×10^4	66.37	22.31	0.33	0.1025	0.58
2	50	100	201	4×10^4	66.37	22.31	0.33	0.1025	0.58
3	100	10	203	4×10^4	66.37	22.31	0.33	0.1025	0.58
4	100	50	203	4×10^4	66.37	22.31	0.33	0.1025	0.58
5	100	100	203	4×10^4	66.37	22.31	0.33	0.1025	0.58
6	100	100	304	4×10^4	66.37	33.46	0.33	0.1025	0.82
7	100	100	152	4×10^4	66.37	16.73	0.33	0.1025	0.56
8	100	100	122	4×10^4	66.37	13.38	0.33	0.1025	0.54
9	100	100	203	1×10^2	0.80	1.32	0.08	0.1806	0
10	100	100	203	6×10^2	4.69	7.19	0.19	0.1602	0
11	100	100	203	2×10^3	13.39	14.66	0.27	0.1475	0
12	100	100	203	1×10^4	32.55	17.90	0.29	0.1153	0.34
13	100	100	203	9×10^4	99.06	22.31	0.33	0.1013	0.93
14	100	100	203	2×10^5	168.24	22.31	0.33	0.0897	1.14

and σ is the surface tension coefficient and is assumed to be a constant.

C. Front tracking

After the fluid velocity is solved on the regular finite difference grid, the velocity of the moving interface (or “front”) is computed by interpolating the velocities from the surrounding fixed grids. The front is then advected normally in a Lagrangian manner,

$$\mathbf{x}_f^{n+1/2} = \mathbf{x}_f^n + \mathbf{u}_f^n \frac{\Delta t}{2}, \quad (16)$$

$$\mathbf{x}_f^{n+1} = \mathbf{x}_f^{n+1/2} + \mathbf{u}_f^{n+1} \frac{\Delta t}{2}, \quad (17)$$

where \mathbf{u}_f is the front velocity, \mathbf{x}_f denotes the position of the front, n represents the current time step, and $n+1$ is for the next step. This motion of the interface is second-order accurate. After the interface moves to a new location, both redistribution of the marker points and conservation of the bubble volume are simultaneously enforced using a level contour reconstruction procedure [32].

III. RESULTS AND DISCUSSION

In this section, two validation studies including a rising bubble and a rising Taylor bubble are first presented. Investigations on the characteristics of a Taylor bubble rising due to the changes in density ratio (η), viscosity ratio (λ), Eötvös number (Eo), and Archimedes number (Ar) are presented and discussed. Table II lists a summary of cases studied and the results. The numerical studies are in the ranges of $25 < \eta < 100$, $10 < \lambda < 100$, $122 < \text{Eo} < 304$, and $100 < \text{Ar} < 2 \times 10^5$. Whenever possible, the results are compared with the existing ones.

A. Validation on single spherical bubble rising in quiescent viscous liquids

The first validation case is a single spherical bubble rising in quiescent viscous liquids. The simulated steady-state shapes are displayed together with the regime map of a bubble rising [34,35] in Fig. 2. The three simulation cases spread into three different flow regimes, namely, spherical, oblate ellipsoidal cap, and disk-shaped ellipsoidal. The Eötvös number (Eo), Morton number (Mo), density ratio (η), and viscosity ratio (λ) for the three cases are

- (i) $\text{Eo}=3.1$, $\text{Mo}=1.2 \times 10^{-1}$, $\eta=100$, $\lambda=100$;
- (ii) $\text{Eo}=327.0$, $\text{Mo}=36.3$, $\eta=100$, $\lambda=100$; and
- (iii) $\text{Eo}=32.7$, $\text{Mo}=1.4 \times 10^{-4}$, $\eta=100$, $\lambda=100$.

Here, the characteristic length for Eo is the diameter of the initial spherical bubble.

According to Mukundakrishnan *et al.* [28], when $R^* \geq 3$ (where $R^*=R/2r_0$), the domain can be considered as an infinite medium and the effect of the sidewalls is minimal. Therefore, the cylindrical computational domain employed for this study has the dimensions of $R=0.03$ m, $H=0.30$ m, and the bubble has a radius of $r_0=0.005$ m. At the initial state, the spherical bubble is located at $4r_0$ from the bottom of the wall and both liquid and bubble are assumed to be stationary.

The shape evolutions for the three simulated cases are illustrated in Fig. 3. The steady-state shapes of the three cases are represented by the black-filled geometries. At this stabilized shape, the bubble travels at fixed Reynolds (Re_T) and Weber (We_T) numbers. The summary of Re_T and We_T are listed on top of Fig. 3. Re_T 's are compared against the Reynolds number of regime map, as shown in Fig. 2, with a good agreement. In addition, under the same flow regime, the simulated shape is the same as that designated from the regime map, indicating that the terminal shapes are well predicted.

B. Validation on a Taylor bubble rising in viscous liquid

The second validation case is based on experimental work by Nogueira *et al.* [3,15] on a Taylor bubble rising in viscous

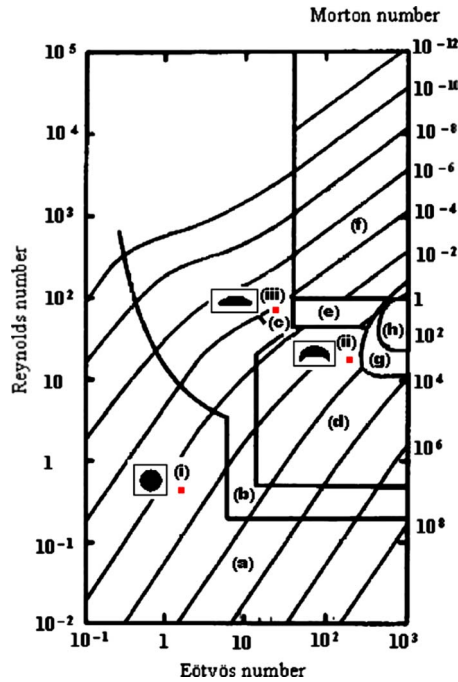


FIG. 2. (Color online) The regime map of experimentally observed terminal shapes of single spherical bubble rising in different flow regimes: (a) spherical, (b) oblate ellipsoidal, (c) disk-shaped ellipsoidal, (d) oblate ellipsoidal cap, (e) spherical cap with closed and steady wake, (f) spherical cap with open and unsteady wake, (g) smooth and steady skirted shape, and (h) wavy and unsteady skirted shape [34,35]. In the figure, three filled squares together with simulated shapes represent three simulations conducted: (i) $Eo=3.1$, $Mo=1.2 \times 10^{-1}$; (ii) $Eo=327.0$, $Mo=36.3$; and (iii) $Eo=32.7$, $Mo=1.4 \times 10^{-4}$.

liquid. In the experiment, a Taylor bubble rose in a 0.032 m internal diameter tube filled with aqueous glycerol with a density of 1222 kg/m³ and a dynamic viscosity of 0.109

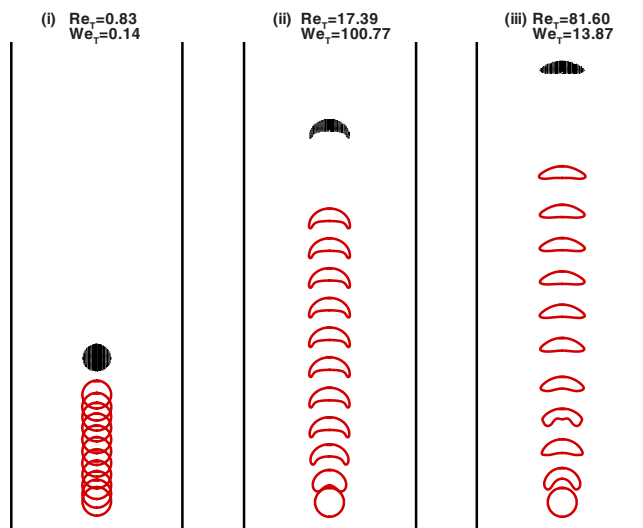


FIG. 3. (Color online) The simulated bubble shapes for (i) $Eo=3.1$, $Mo=1.2 \times 10^{-1}$; (ii) $Eo=327.0$, $Mo=36.3$; and (iii) $Eo=32.7$, $Mo=1.4 \times 10^{-4}$. In these cases, the density ratio and viscosity ratio are set to $\eta=100$ and $\lambda=100$, respectively.

kg/ms. These experimental conditions correspond to an Archimedes number (Ar) of 4×10^4 . The measured bubble velocity was 0.197 m/s, corresponding to a Froude number (Fr) of 0.35. The thin liquid film thickness (w) was 0.00327 m, i.e., $0.1022D$ and the wake length (l_w) was $0.38D$ (see Fig. 4 for the definition of l_w). Two simulation cases according to the experimental conditions are conducted: one with bubble length (L_0) of $4r_0$ and the other is with $5r_0$. Figure 4(c) shows an enlarged view of Fig. 4(a) near the tail region. The velocity vectors are displayed without any skipping of grids in radial direction while they are shown by skipping three points in Figs. 4(a) and 4(b), and compared to Figs. 4(a) and 4(b) the velocity vectors in Fig. 4(c) are plotted by skipping less grids in the rising direction. The flow in the thin-film region and the vortical structures inside the bubble and at the wake are more clearly observed.

In Fig. 4, the flow field including vectors and streamlines of the two cases are plotted at the reference frame moving with the bubble nose at the final steady state. The bubble feels a uniform surrounding flow coming toward it with a speed of the terminal velocity (U_T), and the Reynolds number based on U_T is 66.37. The surrounding fluid then flows into the thin film between the bubble and the wall (as the two fluids are immiscible). To satisfy the continuity equation, the flow inside the thin film is accelerated and the pressure is decreased. Once the fluid flow exits the thin film near the tail of the bubble, it experiences an adverse pressure gradient. As a result, a vortex is formed at the wake of the bubble.

The interface moves with nearby fluid to ensure no mixing of two fluids. Similar constraint was also discussed by [36] as a boundary condition for a moving fluid interface to satisfy no normal flow of fluid from or into the interface. The fluid on the interface near the wall moves downward and, due to the viscosity, the fluid near the interface inside the bubble also flows downward. However, when this fluid reaches the tail of the bubble, it turns around to conserve the mass of the bubble. This leads to a rotational flow inside the bubble.

Three parameters, namely, Fr , w , and l_w , are compared with the existing theoretical and/or experimental works. For both cases, Fr is 0.33, where Fr corresponds to C in Eq. (1). This value falls within the range of the constant C listed in Table I. In addition, the value of $Fr=0.33$ is of 6% discrepancy compared to that measured by Nogueira *et al.* [15]. Second, the simulated w has the value of $0.1025D$ with a difference less than 1%, comparing to the result by Nogueira *et al.* [15]. A theoretical equation assessing the thickness of the stabilized film was proposed by Brown [19] as below,

$$w = \left(\frac{3\mu_l U_T (R - w)}{2g\rho_l} \right)^{1/3}.$$

Calculated from the equation, w is 0.00319 m or $0.0997D$, which is 3% lower than that of the numerical prediction. Lastly, the wake length (l_w) determined from this study is $0.58D$, which is approximately 30% larger than the measurement by Nogueira *et al.* [3]. However, from the empirical equation proposed by Campos and Guedes De Carvalho [14], as given below,

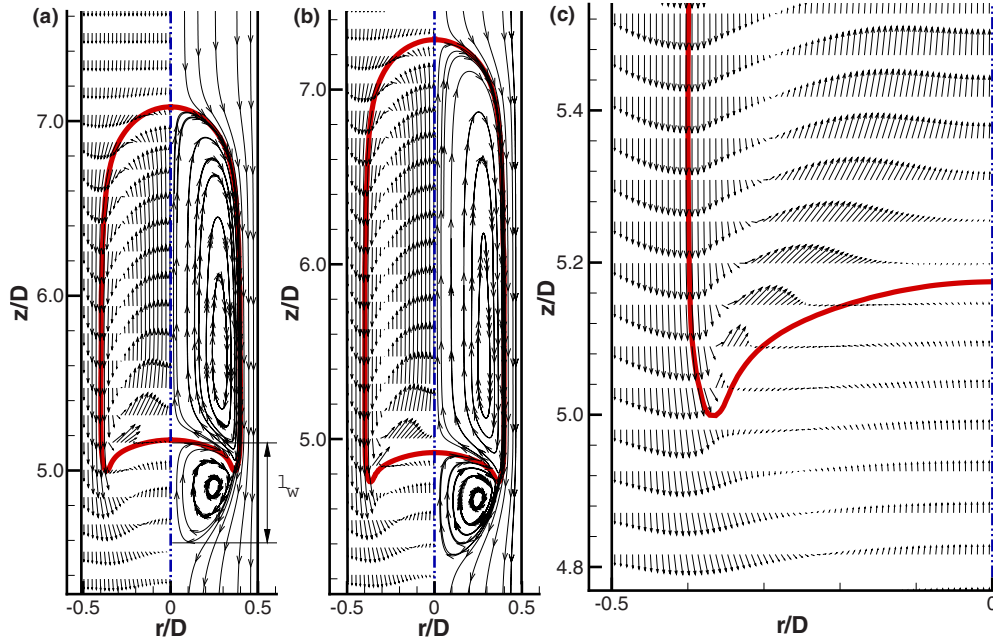


FIG. 4. (Color online) Velocity vectors (left half) and streamlines (right half) of a rising Taylor bubble at a frame of reference moving with the bubble nose. (a) $L_0=4r_0$, (b) $L_0=5r_0$, and (c) enlarged view of (a) near the tail region.

$$\frac{l_w}{D} = 0.30 + 1.22 \times 10^{-3} (gD^3)^{1/2} \rho_l / \mu_l,$$

the l_w calculated is $0.55D$, which is approximately 5% lower than those simulated in this study.

In addition, it is noted that despite having different bubble lengths, both cases reveal the same Froude number (Fr), thin liquid film thickness (w), and wake length (l_w). This conclusion is supported by Kawaji *et al.* [23]. In their work, the bubble of different lengths was found to have the same terminal speed.

The numerical scheme is well validated by the various cases conducted earlier. Moreover, the second validation proffers that the effect of bubble length has minimal effect on the bubble characteristics. Therefore, we shall employ the numerical scheme to perform parametric studies of a Taylor bubble with initial length of $4r_0$ rising in stagnant liquids.

C. Effects of density and viscosity ratios

In order to investigate the effect of the density ratio (η) on Taylor bubble behavior, three cases are simulated with density of the bubble 25, 50, and 100 times smaller than that of liquid, denoted as cases 1, 2, and 5, respectively, in Table II. In these three cases, other parameters such as viscosity ratio (λ), Eötvös number (Eo), and Archimedes number (Ar) remain almost the same, i.e., $\lambda=100$, $Eo \approx 200$, and $Ar=4 \times 10^4$. The shapes and the flow fields for the cases are shown in Fig. 5. The thin liquid film thickness (w) is $0.1025D$, $l_w=0.58D$, and $Fr=0.33$ for all the cases. Within the range of study conducted, it is found that the density ratio has minimal effect on the bubble shape, the thin liquid film thickness, as well as the wake length.

Three viscosity ratios, namely, 10, 50, and 100, are simulated to examine the effect of the viscosity ratio. These three

cases correspond to cases 3, 4, and 5 in Table II and it is noted that the other parameters (η , Eo , and Ar) remain unchanged. Comparison between these cases in terms of the shape and flow field is displayed in Fig. 6. For these three cases, all have the same final bubble shape, Froude number ($Fr=0.33$), thin liquid film thickness ($w=0.1025D$), and wake length ($l_w=0.58D$).

All the six cases reveal the same Reynolds (Re_T) and Weber (We_T) numbers, i.e., 66.37 and 22.31, respectively. The selected density and viscosity ratios lead to small variation in nondimensional numbers (Eo and Ar), which therefore gives minimal effects in the bubble dynamics, as ex-

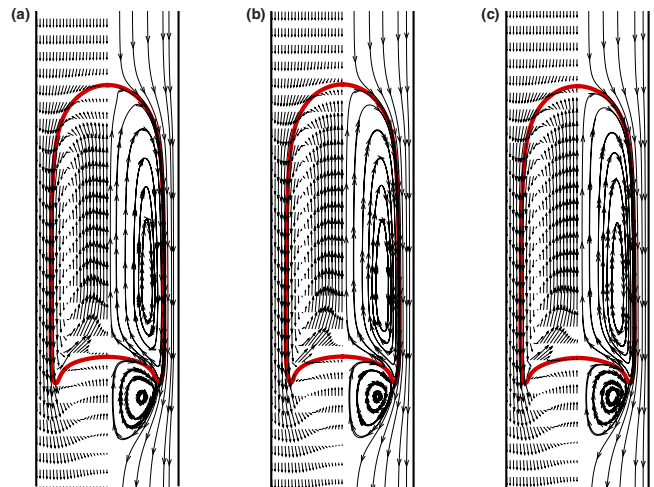


FIG. 5. (Color online) Effect of density ratio (η) on the bubble terminal shapes, velocity vectors (left half), streamlines (right half), and wake lengths. (a) $\eta=25$ (case 1), (b) $\eta=50$ (case 2), and (c) $\eta=100$ (case 5).

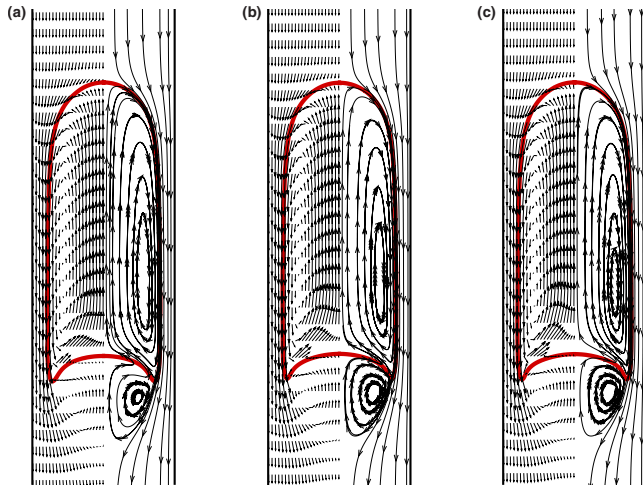


FIG. 6. (Color online) Effect of viscosity ratio (λ) on the bubble terminal shapes, velocity vectors (left half), streamlines (right half), and wake lengths. (a) $\lambda=10$ (case 3), (b) $\lambda=50$ (case 4), and (c) $\lambda=100$ (case 5).

pected. Our simulations further assure the approximation made by Lu and Prosperetti [26].

D. Effect of Eötvös number

By changing the Eötvös number (Eo), it varies the relative strength between buoyancy forces and surface tension forces. In order to study the effect of Eo on the dynamics of a Taylor bubble, four simulation cases are conducted with the density ratio (η), viscosity ratio (λ), and Archimedes number (Ar) fixed. The simulation conditions and the results are compiled in Table II where the Eötvös numbers for the four cases are 122, 152, 203, and 304. The final Taylor bubble shapes and flow fields for all cases are shown in Figs. 7(a)–7(d).

From Table II, with increasing of Eo , We_T is increased from 13.38 to 33.46. Larger We_T implies that in comparison

to surface tension forces, the inertial forces become more dominant and the interface is easier to deform. The surface tension forces significantly affect the level of concavity at the rear of Taylor bubble. As an observation of Fig. 7(a), where We_T is the highest among four cases, the tail of the Taylor bubble is elongated and appears to be jagged. Consequently, two wakes are created and the total wake length is calculated as $0.82D$. It should be noted that this tail oscillates, and if the surface tension force is further reduced the tail might be pinched off and satellite bubbles might be created. The wake length for $Eo=203$ is $0.58D$ and is reduced to $0.56D$ for $Eo=152$, and $0.54D$ for $Eo=122$. In contrast, the change in Eo does not significantly affect the dynamics at the nose and the thin-film regions. Therefore, the Taylor bubbles of four cases have the same Re_T of 66.37, the same Fr of 0.33, and the same w of $0.1025D$.

In order to clearly observe the changes at the tail region, an enlarged view of the region is displayed in Fig. 7(e), where the tail tips from the top to the bottom represent a progressive reduction in surface tension forces. For all the cases, We_T is on the order of $O(10)$, which normally indicates large deformation of bubbles or drops and even breakup. However, in Figs. 7(b)–7(d), the tail of the bubble is slightly extended, and in Fig. 7(a) a jump in the elongation of the tail is observed. In order to explain this phenomenon, a Weber number (We_l) based on local curvature and velocity is employed, i.e.,

$$We_l = \frac{\rho_l U_l^2 R_l}{\sigma},$$

where U_l is the liquid velocity near the tip of the tail and R_l denotes the radius at the tip. The values of We_l for the four cases [Figs. 7(a)–7(d)] are 1.90, 1.27, 1.19, and 0.83, respectively. For the three smaller We_l 's, the surface tension forces are sufficiently strong to maintain a slightly dimpled shape. For $We_l=1.90$, the surface tension forces can no longer maintain the dimpled shape, while the inertial forces elon-

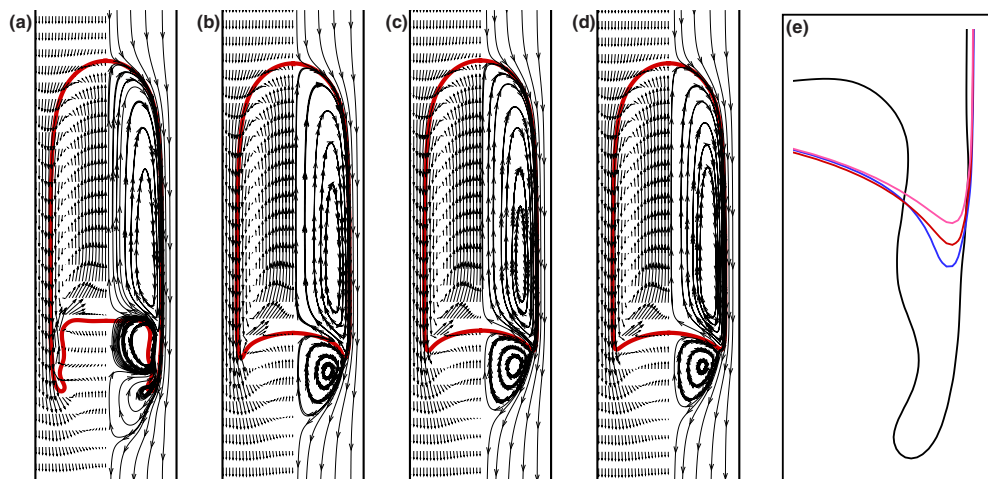


FIG. 7. (Color online) Effect of Eötvös number (Eo) on the bubble shapes and wake patterns. (a) $Eo=304$ (case 6), (b) $Eo=203$ (case 5), (c) $Eo=152$ (case 7), and (d) $Eo=122$ (case 8). At a frame of reference moving with the bubble, vectors (left half) and streamlines (right half) of each figure show the velocity field within and around each Taylor bubble. The enlarged view at the tail regions for different Eo 's is given in (e). The tail tips from the top to the bottom represent a progressive reduction in surface tension forces.

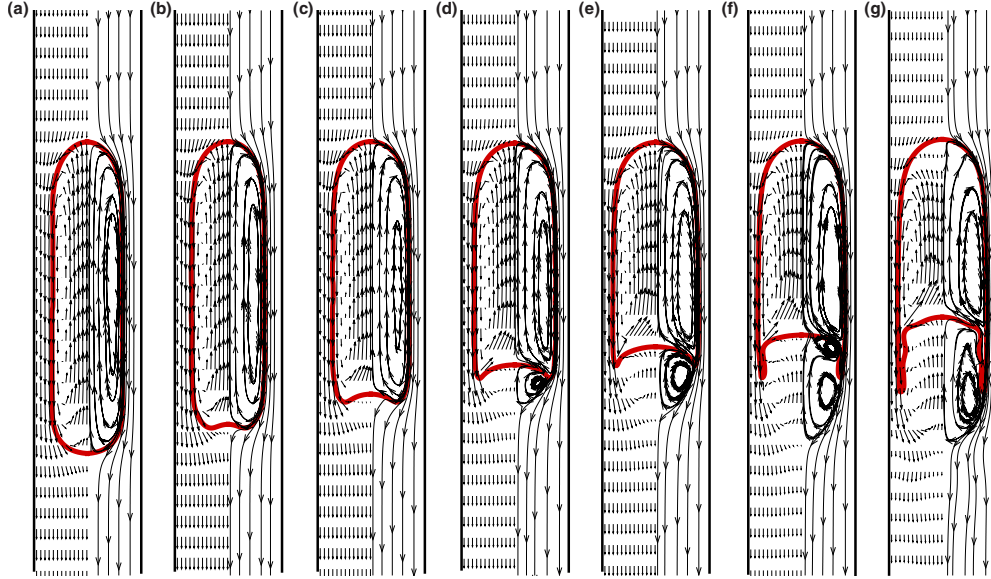


FIG. 8. (Color online) Final shapes and wake structures under the effect of Archimedes number (Ar): (a) $Ar=1 \times 10^2$ (case 9), (b) $Ar=6 \times 10^2$ (case 10), (c) $Ar=2 \times 10^3$ (case 11), (d) $Ar=1 \times 10^4$ (case 12), (e) $Ar=4 \times 10^4$ (case 5), (f) $Ar=9 \times 10^4$ (case 13), and (g) $Ar=2 \times 10^5$ (case 14). In each figure, the left half provides vectors at a frame of reference moving with the bubble and on the right half, it shows the corresponding streamlines.

gate the tail and a skirted bubble is obtained. The critical We_T for this sudden change is around unity.

E. Effect of Archimedes number

In order to investigate the effect of Ar on Taylor bubble behavior, seven cases are conducted with the same density ratio (η) of 100, viscosity ratio (λ) of 100, and Eötvös number (Eo) of 203. The simulation conditions and results for the seven cases are listed in Table II, where Ar is varied from $O(10^2)$ to $O(10^5)$. The transformations of final shapes and wake structures of the Taylor bubble for the seven cases are presented in Fig. 8.

For the case in Fig. 8(a), Ar is the lowest and the Taylor bubble encounters the highest resistance from the surrounding fluid. As a result, the Taylor bubble rises at the lowest terminal velocity, i.e., $Fr=U_T/(gD)^{1/2}=0.08$ and possesses the lowest We_T . In addition, higher viscous shear forces from the surrounding liquid also facilitate the elongation of the bubble. As it can be seen in Fig. 8(a), the final shape of the bubble is long bullet shaped with rounded leading and trailing edges. Also, the cylindrical body of the Taylor bubble is the longest and, as a consequence, the thin film turns out to be the thickest. The measured thin-film thickness is $w=0.1806D$.

With the increase in Ar , the surrounding liquid becomes less viscous. This leads to a higher Fr , but the trend only happens for $Ar < 4 \times 10^4$, above which Fr remains constant and so does We_T . A log-log plot showing the relationship between Fr and Ar was presented in the open literature [37]. In the paper, the correlations were converted from approximately 250 experiments on the rise velocity of long gas bubbles for fixed ranges of Eo . As this numerical study is focusing on $Eo > 40$, the following expressions are adopted for comparison:

For ($Ar < 1.6 \times 10^3$),

$$Fr = (9.221 \times 10^{-3} Ar^{0.4885}).$$

For ($Ar \geq 1.6 \times 10^3$),

$$Fr = 0.341.$$

It should be noted that $Ar=Re_B^2$ (Re_B was employed by Viana *et al.* [37]). As indicated in Fig. 9(a), the simulated results are in good agreement with the correlations, while the simulations have a rather smooth transition. However, from Table II, Re_T is noted to increase continuously with Ar . This is not only due to the increase in the terminal velocity (for $Ar < 4 \times 10^4$) but also due to the decrease in the liquid viscosity.

As the viscous forces become weaker, the Taylor bubble develops from a long and slender shape into a shorter and fatter figure, squeezing the thin liquid film into a narrower region. Therefore, w/D decreases, as given in Table II. In order to obtain a correlation between w/D and Ar , the data are curve fitted and plotted in a log-log format, as shown in Fig. 9(b), where symbols are numerical results and the solid line represents the fitted correlation. The correlation is

$$\frac{w}{D} = 0.32 Ar^{-0.1}. \quad (18)$$

It is noted that a remarkable change happens at the rear of the bubble with Ar . For $Ar=1 \times 10^2$, the Taylor bubble has a rounded trailing edge. When Ar progressively changes from 6×10^2 to 4×10^4 , the bottom of the Taylor bubble becomes dimpled and indentation increases with Ar . For the cases where Ar is on the order of $O(10^5)$, the tail is skirted. The flow separation is initiated at $Ar=1 \times 10^4$, which corresponds to $Re_T=32.55$. Below which, no noticeable flow separation at the tail region is observed. This also indicates that the flow separation happens at Re_T between 13.39 and 32.55. In com-

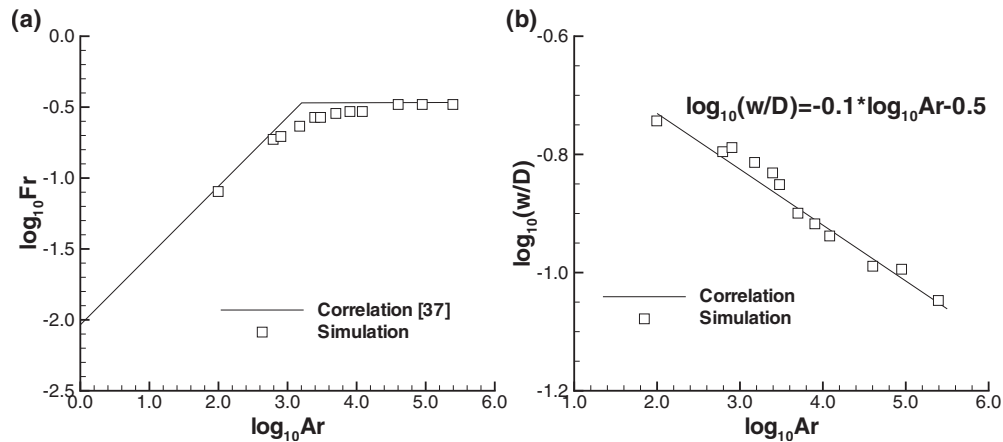


FIG. 9. (a) Comparison of simulated results with the correlations from Viana *et al.* [37] for cases where $Eo > 40$. (b) Correlation between w/D and Ar .

parison, the onset of flow separation for the steady flow past a sphere occurs at Reynolds number about 24 [38]. The wake length l_w increases from 0.34 ($Ar=1 \times 10^4$, $Re_T=32.55$) to 1.14 ($Ar=2 \times 10^5$, $Re_T=168.24$). The increase in wake length is partially due to the elongation of the tail. In order to clearly observe the evolution of the tails, an enlarged view at the tail regions is demonstrated in Fig. 10, where the lines from the top to the bottom represent the increase in Ar . Again, to explain the underlying physics, We_l 's are calculated as 0.11, 0.29, 0.77, 1.29, 1.50, and 2.33, respectively. The critical We_l is found to be around unity. Figure 11 shows a phase diagram for different tail shapes in Eo and Ar space, where the filled triangles are the results of Lu and Prosperetti [26]. Wavy tails occur for large Eo and Ar , and for small values the tails are steady. Our prediction agrees well with Lu and Prosperetti's [26] results, except for Eo of 203 and Ar of 2.3×10^4 . It is believed that the gas inside the Taylor

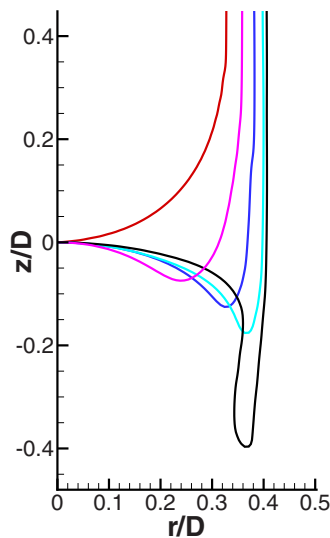


FIG. 10. (Color online) Enlarged view of the tails for different Ar 's. The lines from the top to the bottom represent cases in Fig. 8 with Ar 's of 1×10^2 , 2×10^3 , 1×10^4 , 4×10^4 , and 9×10^4 , and the corresponding We_l 's are 0.11, 0.29, 0.77, 1.29, and 1.50, respectively.

bubble might be a key factor for the difference.

The information of wall shear stress is important, especially to water treatment industry using membrane technology, where an optimized wall shear stress is always desired. This is because a lower wall shear stress is unable to disrupt the concentration polarization layer buildup at fiber surface, while a higher wall shear stress may damage the surface chemistry of the membrane fiber which subsequently shortens the fiber life span. Either situation increases the operating costs. Figure 12(a) provides the change in wall shear stress under the effect of Ar . In Fig. 12(a), a factor of $\rho_l g D$ is introduced to normalize the wall shear stress (τ_w). The tube diameter D is utilized to nondimensionalize the distance (z), where $z/D=0$ signifies the bubble nose. It is noted that increasing Ar results in a reduction in the wall shear stress. This is because higher Ar represents less viscous liquid and the lower viscosity of liquid contributes to a lower wall shear stress. It can also be seen that lower Ar has a longer Taylor bubble and a flat wall shear stress within the thin film, while higher Ar results in a shorter Taylor bubble and a continuous increase in wall shear stress toward the tail. In addition, it is noted that, for the highest Ar , there is a jump in the wall shear stress near the tail. The disturbance is believed to be caused by jagged and wavy tail of Taylor bubble created

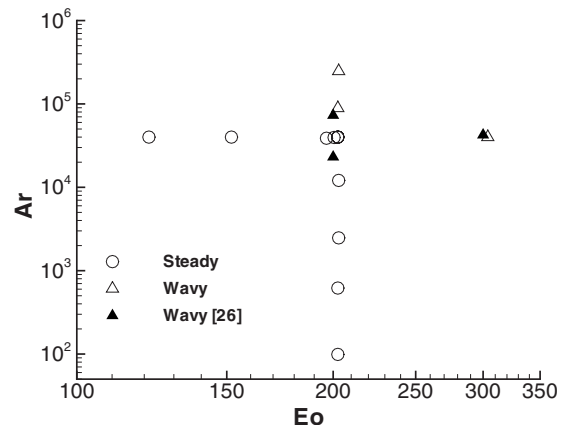


FIG. 11. Phase diagram of the tail shape in Eo and Ar space of a Taylor bubble rising in a quiescent fluid.

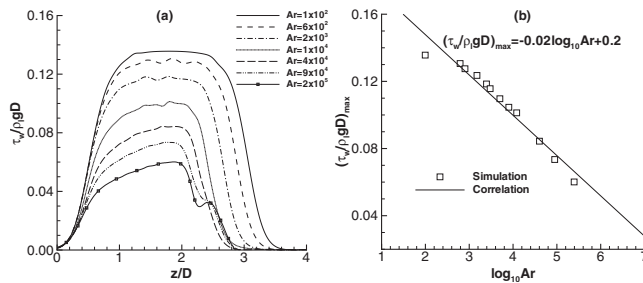


FIG. 12. (a) Wall shear stress under the effect of Ar. $z/D=0$ represents the bubble nose. (b) Maximum value of wall shear stress versus $\log_{10} Ar$.

under higher Ar scenario. Figure 12(b) shows the correlation between the maximum wall shear stress versus Ar, where the symbols are the simulated results and the line is curve fitted. It is found that

$$\left(\frac{\tau_w}{\rho_l g D} \right)_{max} = -0.02 \log_{10} Ar + 0.2. \quad (19)$$

IV. CONCLUSIONS

In this paper, a front tracking methodology using a cylindrical coordinate system is utilized to investigate the behavior of a Taylor bubble rising in stagnant liquids. The front tracking algorithm is validated against single bubble rising in quiescent viscous liquids and a Taylor bubble drifting in stagnant viscous liquid, with good agreement. After verification, the front tracking algorithm is used to investigate the effects of density ratio (η), viscosity ratio (λ), Eötvös number (Eo), and Archimedes number (Ar) on the dynamics of a rising Taylor bubble. The simulation results show that η and

λ have minimal effect on the Taylor bubble final shape, the Reynolds number (Re_T), the Weber number (We_T), the Froude number (Fr), the thin liquid film thickness (w), and the wake length (l_w). Eo and Ar play a significant role in determining the elongation of tail and the wake structures created therein, where higher Eo and Ar result in longer l_w . In order to elucidate the sudden jump in the elongation of the tail, a Weber number (We_T) based on local curvature and velocity is evaluated and it is found that the sudden elongation occurs at We_T around unity. Re_T , Fr, and w appear to be unaffected under the effect of Eo, but these parameters change drastically with Ar. Increasing of Ar results in an increase in Re_T . At Re_T between 13.39 and 32.55, the flow separation is initiated, and when $Re_T > 32.55$ the l_w increases with Ar. Fr and We_T are also found to increase with Ar, but only for Ar below 4×10^4 ; above which, constant values of Fr=0.33 and $We_T=22.31$ are obtained. In addition, increasing of Ar transforms a longer and slender Taylor bubble into a shorter and fatter Taylor bubble and, thus, the thin liquid film thickness is reduced. A correlation between the thin-film thickness (w/D) and the Archimedes number (Ar) is obtained as $w/D=0.32 Ar^{-0.1}$. Moreover, increasing Ar results in a reduction in the wall shear stresses, and it is found that the maximum wall shear stress follows $(\tau_w/\rho_l g D)_{max} = -0.02 \log_{10} Ar + 0.2$.

ACKNOWLEDGMENTS

The authors sincerely thank Professor Tapas Kumar Mandal from Indian Institute of Technology, Guwahati and Professor P. K. Das from Indian Institute of Technology, Kharagpur for their willingness to share during the course of this numerical study.

- [1] R. M. Davies and G. I. Taylor, *Proc. R. Soc. London, Ser. A* **200**, 375 (1950).
- [2] S. Nogueira, R. G. Sousa, A. M. F. R. Pinto, M. L. Riethmuller, and J. B. L. M. Campos, *Exp. Fluids* **35**, 598 (2003).
- [3] S. Nogueira, M. L. Riethmuller, J. B. L. M. Campos, and A. M. F. R. Pinto, *Chem. Eng. Sci.* **61**, 7199 (2006).
- [4] T. Taha and Z. F. Cui, *Chem. Eng. Sci.* **61**, 676 (2006).
- [5] P. C. Huzyak and K. W. Koelling, *J. Non-Newtonian Fluid Mech.* **71**, 73 (1997).
- [6] S. R. Bellara, Z. F. Cui, and D. S. Pepper, *Biotechnol. Prog.* **13**, 869 (1997).
- [7] T. Taha and Z. F. Cui, *Chem. Eng. Sci.* **59**, 1181 (2004).
- [8] J. Prothero and A. C. Burton, *Biophys. J.* **1**, 565 (1961).
- [9] C. M. Muth and E. S. Shank, *N. Engl. J. Med.* **342**, 476 (2000).
- [10] D. P. Cavanagh and D. M. Eckmann, *J. Fluid Mech.* **398**, 225 (1999).
- [11] D. W. Rader, A. T. Bourgoynne, Jr., and R. H. Ward, *JPT, J. Pet. Technol.* **27**, 571 (1975).
- [12] K. H. Bendiksen, *Int. J. Multiphase Flow* **11**, 797 (1985).
- [13] G. K. Batchelor, *J. Fluid Mech.* **184**, 399 (1987).
- [14] J. B. L. M. Campos and J. R. F. Guedes De Carvalho, *J. Fluid Mech.* **196**, 27 (1988).
- [15] S. Nogueira, M. L. Riethmuller, J. B. L. M. Campos, and A. M. F. R. Pinto, *Chem. Eng. Sci.* **61**, 845 (2006).
- [16] A. M. F. R. Pinto, M. N. Coelho Pinheiro, S. Nogueira, V. D. Ferreira, and J. B. L. M. Campos, *Chem. Eng. Res. Des.* **83**, 1103 (2005).
- [17] T. K. Mandal, G. Das, and P. K. Das, *Ind. Eng. Chem. Res.* **47**, 7048 (2008).
- [18] D. T. Dumitrescu, *Z. Angew. Math. Mech.* **23**, 139 (1943).
- [19] R. A. S. Brown, *Can. J. Chem. Eng.* **43**, 217 (1965).
- [20] A. D. Laird and D. Chisholm, *Indust. Eng. Chem.* **48**, 1361 (1956).
- [21] S. Polonsky, L. Shemer, and D. Barnea, *Int. J. Multiphase Flow* **25**, 957 (1999).
- [22] T. Taha and Z. F. Cui, *Desalination* **145**, 179 (2002).
- [23] M. Kawaji, J. M. DeJesus, and G. Tudose, *Nucl. Eng. Des.* **175**, 37 (1997).
- [24] J. D. Bugg, K. Mack, and K. S. Rezkallah, *Int. J. Multiphase Flow* **24**, 271 (1998).
- [25] N. V. Ndinisa, D. E. Wiley, and D. F. Fletcher, *Chem. Eng.*

- Res. Des. **83**, 40 (2005).
- [26] X. Lu and A. Prosperetti, *Ind. Eng. Chem. Res.* **48**, 242 (2009).
- [27] G. Tryggvason, B. Bunner, A. Esmaeeli, D. Juric, N. Al-Rawahi, W. Tauber, J. Han, S. Nas, and Y. J. Jan, *J. Comput. Phys.* **169**, 708 (2001).
- [28] K. Mukundakrishnan, S. P. Quan, D. M. Eckmann, and P. S. Ayyaswamy, *Phys. Rev. E* **76**, 036308 (2007).
- [29] J. Hua and J. Lou, *J. Comput. Phys.* **222**, 769 (2007).
- [30] J. B. Bell, P. Colella, and H. M. Glaz, *J. Comput. Phys.* **85**, 257 (1989).
- [31] M. Sussman and E. G. Puckett, *J. Comput. Phys.* **162**, 301 (2000).
- [32] S. Shin and D. Juric, *J. Comput. Phys.* **180**, 427 (2002).
- [33] B. E. Griffith and C. S. Peskin, *J. Comput. Phys.* **208**, 75 (2005).
- [34] R. Clift, J. R. Grace, and M. E. Weber, *Bubbles, Drops, and Particles* (Academic Press, New York, 1978).
- [35] D. Bhaga and M. E. Weber, *J. Fluid Mech.* **105**, 61 (1981).
- [36] A. Ludu, *Nonlinear Waves and Solitons on Contours and Closed Surfaces* (Springer-Verlag, Heidelberg, 2007).
- [37] F. Viana, R. Pardo, R. Yanez, J. L. Trallero, and D. D. Joseph, *J. Fluid Mech.* **494**, 379 (2003).
- [38] G. K. Batchelor, *An Introduction to Fluid Dynamics* (Cambridge University Press, Cambridge, England, 1967).